ACCSCIENCE PUBLISHING

International Journal of Bioprinting

RESEARCH ARTICLE

Personalized 3D-printed TDM/ZrO_2 scaffolds laden with iPSC-derived SOX9$^+$ sclerotomal progenitors for functional osteochondral regeneration

Yuqing Dong[1,2], Zhijun Zhang[3], Fengxiao Zhao[1], Weihua Guo[1,4*], Jingfei Xiong[5], Zhonghan Li[5], and Yuming Zhao[2*]

[1]State Key Laboratory of Oral Diseases and National Clinical Research Center for Oral Diseases, Department of Pediatrics, West China Hospital of Stomatology, Sichuan University, Chengdu, Sichuan, China

[2]Department of Pediatric Dentistry, National Engineering Laboratory for Digital and Material Technology of Stomatology, National Center of Stomatology, National Clinical Research Center for Oral Diseases, Peking University School and Hospital of Stomatology, Beijing, China

[3]Department of Stomatology, School of Clinical Medical, Chengdu Medical College, Chengdu, Sichuan, China

[4]Yunnan Key Laboratory of Stomatology, The Affiliated Hospital of Stomatology, School of Stomatology, Kunming Medical University, Kunming, Yunnan, China

[5]Key Laboratory of Bio-Resource and Eco-Environment of Ministry of Education, Center of Growth Metabolism and Aging, College of Life Sciences, Sichuan University, Chengdu, Sichuan, China

***Corresponding authors:**
Weihua Guo
(guoweihua943019@163.com)

Yuming Zhao
(yumingzhao70@sina.com)

Citation: Dong Y, Zhang Z, Zhao F, *et al.* Personalized 3D-printed TDM/ZrO_2 scaffolds laden with iPSC-derived SOX9$^+$ sclerotomal progenitors for functional osteochondral regeneration. *Int J Bioprint*. 2025;11(6):531-550. doi: 10.36922/IJB025330333

Received: August 13, 2025
1st revised: September 25, 2025
2nd revised: October 9, 2025
Accepted: October 15, 2025
Published online: October 23, 2025

Abstract

Osteochondral defects resulting from trauma or degenerative diseases are challenging to treat due to the complex hierarchical structure and limited self-healing capacity of articular cartilage. Recent advancements have identified SOX9-positive (SOX9$^+$) sclerotomal progenitors (scl-progenitors), derived from human pluripotent stem cells, as a promising cell source capable of mimicking endochondral ossification and promoting osteochondral regeneration. A personalized three-dimensional (3D)-bioprinted scaffold was developed using treated dentin matrix (TDM)—a decellularized matrix rich in low-crystallinity hydroxyapatite, type I collagen, and osteoinductive factors—as the core bioactive material. To enhance mechanical strength and printability, the TDM was combined with methacrylated gelatin and zirconia nanoparticles. SOX9$^+$ scl-progenitors were encapsulated within the hydrogel matrix and printed using extrusion-based 3D bioprinting to fabricate cell-laden scaffolds with tunable biomechanical and biological properties. The engineered constructs supported robust cell viability, proliferation, and differentiation toward osteochondral lineages *in vitro*. *In vivo* implantation in a nude rat knee osteochondral defect model demonstrated excellent biocompatibility and significant regeneration of both cartilage and subchondral bone tissue. This study presents a translatable and customizable platform integrating stem cell technology, natural biomaterials, and 3D bioprinting for osteochondral tissue engineering. The bioengineered construct offers substantial advantages for personalized osteochondral defect repair over conventional approaches.

***Keywords*:** Osteochondral regeneration; SOX9-positive sclerotomal progenitors; Three-dimensional bioprinting; Tissue engineering; Treated dentin matrix

1. Introduction

Articular cartilage injury represents a pivotal pathological event in the initiation and progression of osteoarthritis.[1] Recent epidemiological studies report that the prevalence of osteoarthritis among individuals over 40 years old in China reaches 46.3%, with a notable trend toward earlier onset in younger populations.[2] Osteochondral tissue is composed of articular cartilage and the underlying subchondral bone, bridged by a layer of calcified cartilage that ensures mechanical integrity and facilitates load transfer across the joint interface.[3] Repairing osteochondral defects remains a formidable clinical challenge due to the distinct biochemical compositions and mechanical properties of its constituent layers, as well as the inherently limited regenerative capacity of cartilage.[4] An epidemiological survey from 2020 indicates that 7.6% of the global population suffers from osteoarthritis, with an increasing number of cases among younger individuals due to inappropriate exercise and repetitive joint overuse.[5] Prolonged mechanical overloading and chronic trauma, often exacerbating joint degeneration, severely impair mobility and quality of life.[2,6] As life expectancy increases and sports-related injuries become more frequent, the demand for effective osteochondral repair strategies continues to grow.

Although current clinical options, such as autologous chondrocyte implantation, remain the gold standard for focal cartilage repair,[7] the limited availability and low proliferative potential of chondrocytes pose significant challenges, as they rapidly lose their functional phenotype in culture and may cause additional donor site damage.[8] Moreover, cartilage lesions are often accompanied by subchondral bone involvement, further complicating the regenerative process and accelerating disease progression.[9,10] Therefore, identifying more effective and feasible osteochondral repair strategies has become a key focus of the current research.

Recent studies have demonstrated the potential of using human pluripotent stem cells (hPSCs) to generate cell types capable of mimicking the natural developmental sequence of osteochondral tissue.[11] Among them, SOX9-positive ($SOX9^+$) sclerotomal progenitors (scl-progenitors) have emerged as a particularly compelling cell population due to their ability to mimic critical stages of endochondral ossification, including mesenchymal condensation, chondrocyte hypertrophy, vascular invasion, and bone marrow cavity formation.[12] These progenitors are derived from hPSCs using a stepwise protocol that faithfully recapitulates embryonic development, yielding over 99% purity across multiple cell lines. Notably, they can be efficiently expanded *in vitro* and directed toward cartilage or bone fates, forming polarized, growth plate-like structures that contribute to cartilage repair *in vivo* without exhibiting undesired hypertrophy or ossification. Compared to mesenchymal stem cells (MSCs) or primary chondrocytes, $SOX9^+$ scl-progenitors display a juvenile-like phenotype, enhanced proliferative potential, and greater resistance to inflammatory cytokines, making them particularly suitable for regenerative applications in aging or osteoarthritic tissues.

However, a limitation in translating these biological advances into clinical practice is the lack of customizable, biomimetic scaffolds capable of integrating mechanical and biological cues for tissue regeneration. As osteochondral defects often vary in size, shape, and location, personalized solutions are essential. In this context, three-dimensional (3D) bioprinting has emerged as a transformative technology that enables the precise fabrication of structurally complex scaffolds tailored to patient-specific anatomy and tissue requirements. To address this, we developed a hybrid osteochondral scaffold by combining treated dentin matrix (TDM)—a natural, bioactive, and mechanically resilient material[13]—with methacrylated gelatin (GelMA) and zirconia (ZrO_2) nanoparticles.

As a decellularized extracellular matrix, TDM retains low-crystallinity hydroxyapatite and a variety of bioactive molecules, including transforming growth factor-β (TGF-β) and bone morphogenetic proteins (BMPs).[14] These components have been shown to efficiently induce MSC differentiation toward both osteogenic and chondrogenic lineages, enhancing tissue regeneration.[15] Numerous *in vitro* and *in vivo* studies have demonstrated that TDM can promote proliferation and lineage-specific differentiation of MSCs into bone- and dentin-forming cells.[16,17] Mechanically, TDM exhibits elastic properties similar to those of calcified cartilage and subchondral bone, along with low immunogenicity and good processability, making it an attractive material for osteochondral scaffold design.[18] Our previous studies demonstrated that TDM exhibits excellent printability when processed into particles less than 40 μm in diameter and combined with suitable excipients.[19] The resulting TDM-based 3D-printed scaffolds provided a favorable microenvironment for cell attachment, proliferation, and differentiation.

Although TDM has been widely explored for osteogenesis and odontogenesis, dentin protein extracts enriched in TGF-β and BMP members have been shown to promote cartilage-like matrix deposition. In line with these findings, we observed that TDM-containing scaffolds released TGF-β3 and BMP-2 at concentrations comparable

to those used in chondrogenic induction media for induced pluripotent stem cell (iPSC)-derived SOX9$^+$ progenitors. This observation provides the rationale for testing TDM as a bioactive component to support chondrogenesis in the present study.

This study aims to develop an effective scaffold for the simultaneous regeneration of articular cartilage and subchondral bone. To achieve this, we used GelMA to enhance the printability and structural stability of TDM, yielding scaffolds with high water content and an interconnected porous network.[20] To reinforce the scaffold further, ZrO_2 was incorporated as a structural additive. ZrO_2 effectively fills the scaffold pores, converting the otherwise brittle and fragile hydrogel network into a mechanically robust, drug-resistant framework that can withstand repetitive mechanical loading and exhibits high resistance to volumetric expansion.[21,22]

Additionally, we employed 3D bioprinting to fabricate a personalized osteochondral scaffold by incorporating iPSC-derived SOX9$^+$ scl-progenitors into TDM/ZrO_2 hydrogel matrices. The resulting bioengineered construct not only offers tunable mechanical properties but also serves as a biologically active platform for supporting stem cell viability, proliferation, and differentiation. We systematically characterized the physical and chemical properties of the scaffolds *in vitro*, and further evaluated their biological performance and regenerative capacity *in vivo* using an osteochondral defect model (Figure 1). This strategy represents a synergistic integration of developmental biology, stem cell engineering, and advanced manufacturing, offering a promising avenue for personalized osteochondral repair.

2. Materials and methods

2.1. Materials

GelMA (degree of substitution: 60%) was purchased from EFL, China. Enzyme-linked immunosorbent assay (ELISA) kits (JL17935-48T, JL25973-48T, JL21985-48T, JL17851-48T) were obtained from J&L Biological, China. Insulin–transferrin–selenium supplement, sodium pyruvate, and Rho-associated protein kinase inhibitors were purchased from Beyotime Biotechnology, China. Basic Dulbecco's Modified Eagle Medium, penicillin–streptomycin, and type II collagenase were purchased from Hyclone, United States. SOX9$^+$ scl-progenitors were obtained from Professor Zhonghan Li, School of Life Sciences, Sichuan University, as described in our previous study.[12]

The experimental animals (nude rats [n=36], male, 6–8 weeks, 200–250 g) were purchased from Ensiweier Biotechnology Co., Ltd., China. All animals were housed under specific pathogen-free conditions with a 12 h light/dark cycle, a temperature of 22 ± 2°C, and a relative humidity of 55 ± 10%. All experimental procedures were approved by the Institutional Animal Care and Use Committee of West China Hospital (ethics approval number: WCHSIRB-D-2023-309) and complied with the National Institutes of Health guidelines for the care and use of laboratory animals.

2.2. Preparation of bioprinting inks

The TDM used in this experiment was prepared according to the method established in a previous study.[23] The samples were then freeze-dried for 8 h and ground into powder passing through a 40 μm sieve.

A 10% (w/v) GelMA-60 solution was prepared by dissolving GelMA in phosphate-buffered saline (PBS) solution at 60°C under continuous stirring, followed by sterilization through a 0.22 μm filter. The bioinks were prepared by mixing the GelMA solution with ZrO_2 nanoparticles (particle size <100 nm) and TDM powder at ratios specified in Table 1.

Mixtures were homogenized using a magnetic stirrer for 30 min at room temperature until uniformly dispersed. Printing was performed using a 3D bioplotter (EnvisionTEC 3D-Bioplotter, Germany) equipped with a low-temperature print head (25°C). The extrusion pressure was set at 2.5 bar, and the printing speed was 8 mm/min. Immediately after printing, constructs were photocrosslinked under a 405 nm UV lamp for 30 s.

2.3. Scaffold characterization

2.3.1. Scanning electron microscopy

Printed scaffolds were freeze-dried for 24 h, cut into cross-sections, and sputter-coated with gold (10 nm thickness) using a Quorum SC7620 ion sputter coater (manufacturer, country). Samples were observed using a Zeiss Sigma 500 scanning electron microscope (Carl Zeiss, Germany) under high vacuum (1×10^{-5} mbar) at an accelerating voltage of 20 kV. Pore morphology and distribution were recorded at various magnifications.

Table 1. Composition of methacrylated gelatin-based bioinks

Groups	Reagent
0 % TDM	0.05 g ZrO2; 1 mL 10 % GelMA-60
30 % TDM	0.05 g ZrO2;1 mL 10 % GelMA-60
50 % TDM	0.05 g ZrO2; 1 mL 10 % GelMA-60
70 % TDM	0.05 g ZrO2; 1 mL 10 % GelMA-60

Abbreviations: GelMA, methacrylated gelatin; TDM, treated dentin matrix; ZrO_2, zirconia.

2.3.2. Fourier transform infrared spectroscopy

Scaffolds were ground into powder (<200 μm) and analyzed using a Bruker EQUINOX 55 Fourier transform infrared (FTIR) spectrometer (Bruker, Germany) in attenuated total reflectance mode. Spectra were recorded in the range of 400–4000 cm^{-1} at a resolution of 4 cm^{-1} with 32 scans per sample.

2.3.3. X-ray diffraction

The treatment method for the scaffolds was similar to that described in **Section 2.3.2**. The crystal phase analysis of the scaffold was performed using an X-ray diffractometer (manufacturer, country). The scanning angle range was selected from 5–85°, and detection was carried out at a scanning rate of 5°/min. Jade software (developer, country) was used to analyze and process the X-ray diffraction data, and phase characterization was based on the principle of the three strongest peaks.

2.3.4. Mechanical test

A Shimadzu universal testing machine (manufacturer, country) was used to conduct compression and tensile tests on the scaffolds. Cylindrical (diameter = 0.8 cm, height = 1 cm) and rectangular (0.4×1×3 cm) specimens were tested (n = 4) per group. The stroke was set to 0.8 cm (the height limit of the instrument was 0.2 cm), and the descending speed was 0.1 mm/s (n=4).

2.3.5. Degradation test

Quadruplicate scaffold samples were placed in a 12-well plate containing 1 mL of PBS, and the test was performed in a 37°C constant-temperature shaker at 1, 7, 14, 21, and 28 days. The scaffolds were freeze-dried and weighed on days 21 and 28, and the mass loss of the scaffold samples was quantified. The remaining mass of the scaffold after freeze-drying for different time points was calculated to evaluate its degradation rate. The scaffold material degradation rate (Q_d) was calculated using the following formula (**Equation (1)**):

$$Q_d = \frac{(W_0 - W_d)}{W_0} \times 100\% \quad (1)$$

where W_0 is the initial mass of the scaffold and W_d is the remaining mass of the scaffold after freeze-drying (n=4).

2.3.6. Swelling test

Quadruplicate scaffolds were freeze-dried, soaked in PBS at 37°C, and weighed at six time points: 1, 2, 4, 8, 12, and 24 h. The swelling ratio (SR) can be calculated as follows (**Equation (2)**):

$$SR = \frac{(W_S - W_d)}{W_d} \times 100\% \quad (2)$$

where W_s and W_d represent the weights of the scaffolds before and after freeze-drying, respectively, indicating the mass change of the scaffold after water absorption (n = 4).

2.3.7. Enzyme-linked immunosorbent assay

Scaffolds were incubated in PBS at 37°C. At weeks 1, 2, 3, and 4, extracts were collected after centrifugation at 5000 rpm for 5 min. Proteins released from the scaffolds were quantified using ELISA kits following the manufacturer's protocol. Each group was tested in quadruplicate[24] (n = 6).

2.4. *In vitro* studies

2.4.1. Culture and induction of differentiation of SOX9+ sclerotomal progenitors

After obtaining human fibroblasts for genetic reprogramming, a cell line was established by inserting the fluorescent reporter gene tdTomato downstream of *SOX9* to enable cell screening and polymerase chain reaction (PCR)-based detection of related gene expression. Sclerotome-like cells were obtained following genetic reprogramming and induction of differentiation. Owing to their high expression of *SOX9*, these cells were designated as SOX9+ scl-progenitors in this study. The detailed cell culture and induction protocols have been described in our previous study.[12]

2.4.2. Cytocompatibility testing of scaffolds

Scaffolds were placed in 24-well plates, and cells were seeded onto the scaffold surfaces at a density of 5×10^3 cells per well. Subsequently, the scaffolds were transferred to transwell inserts, and the culture medium was added to fully submerge them, allowing co-culture under standard conditions. After 1, 3, 5, and 7 days of co-culture, the medium was removed, and 500 μL of Cell Counting Kit-8 reagent (manufacturer, country) was added to each well to ensure complete immersion of the scaffolds. The plates were incubated at 37°C in the dark for 1 h. Following incubation, the supernatants were transferred to 96-well plates, and absorbance was measured at 450 nm using a microplate reader (manufacturer, country).

Live/dead staining was performed using the same co-culture method. After the designated incubation period, the scaffolds were inverted and placed at the bottom of confocal dishes, and imaging was performed using confocal microscopy to assess cell viability and distribution (n=4).

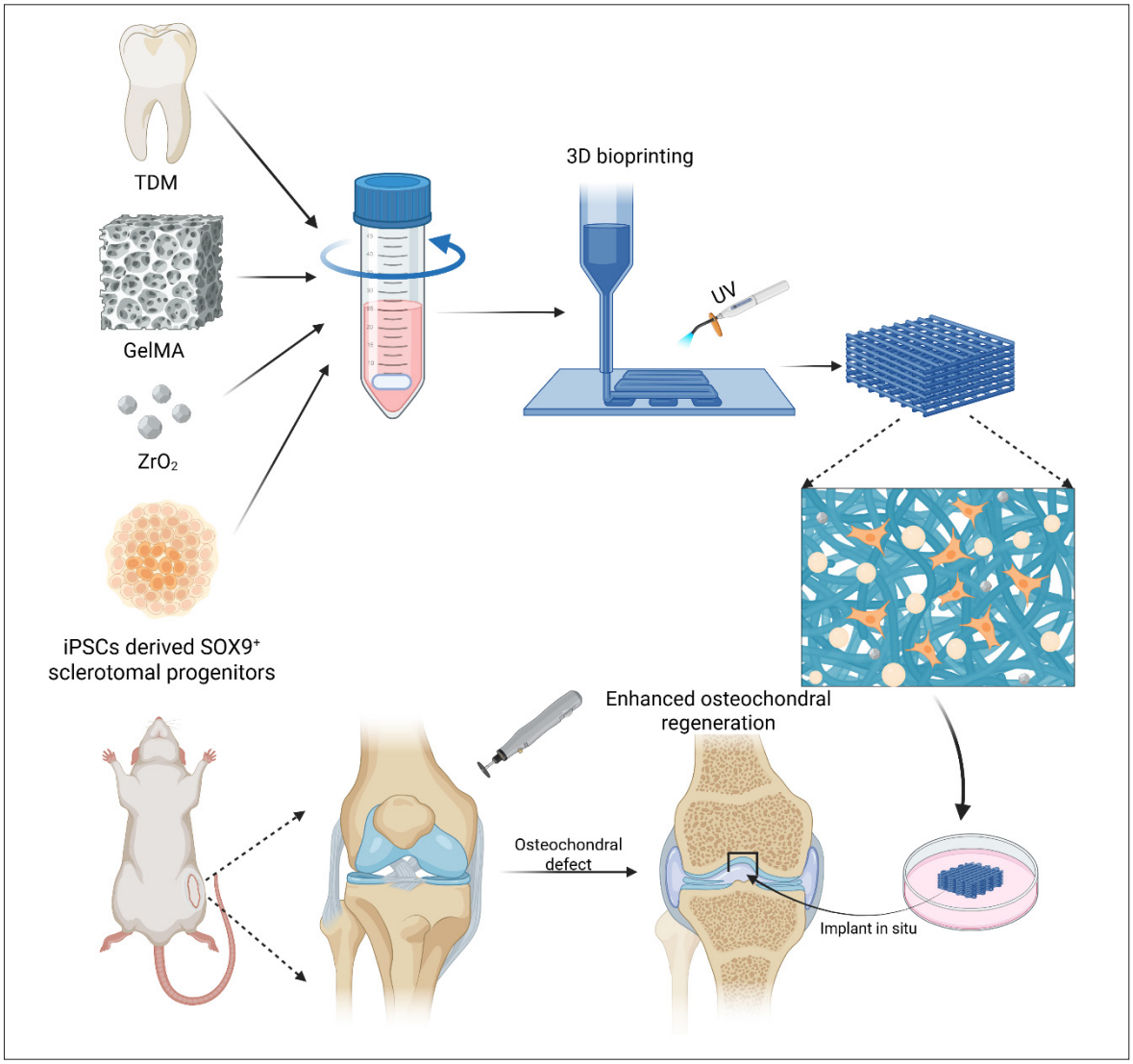

Figure 1. Schematic diagram of TDM/ZrO_2 hydrogel scaffold for osteochondral defect regeneration. Abbreviations: 3D, three-dimensional; GelMA, methacrylated gelatin; iPSC, induced pluripotent stem cell; Scl, sclerotomal; TDM, treated dentin matrix; UV, ultraviolet; ZrO_2, zirconia.

2.4.3 Effect of scaffold material on gene expression in iPSC-derived SOX9⁺ scl-progenitors

The iPSC-derived SOX9⁺ scl-progenitors were co-cultured with the scaffolds for seven days, and RNA and protein were extracted for quantitative reverse transcription PCR and Western blot analysis, respectively. Real-time quantitative PCR was performed using a LightCycler PCR System (Roche, Switzerland) with SYBR qPCR Master Mix (manufacturer, country). The cycle threshold (Ct) values were recorded after each reaction and analyzed using the $2^{-\Delta\Delta Ct}$ method with β-actin as the loading control. Primer sequences are provided in Table S1. All experiments were performed in triplicate (n=6).

2.5. *In vivo* studies

2.5.1. Implantation in situ

A nude rat knee joint defect model was established to evaluate the scaffold performance *in vivo*. The cell-loaded bioink was prepared from a cell suspension concentration of 1 × 10^8 cells/mL, with temperature maintained at 30 ± 2°C, printing speed set at 8 mm/s, and air pressure at 1.5–2 bar. Cylindrical scaffolds (diameter: 2 mm; height: 1.5 mm) were printed according to the defect model, photocrosslinked, and preconditioned in complete Dulbecco's Modified Eagle Medium before implantation. A cylindrical defect (diameter: 2.0 mm; depth: 1.5 mm)

was created in the femoral intercondylar fossa of the rat knee using a dental handpiece-mounted trephine under continuous sterile saline irrigation.[25] The printed scaffolds were then implanted into the prepared defects of the nude rat knees and observed *in vivo* for 6 and 12 weeks (n=4).

2.5.2. Micro-computed tomography imaging evaluation and histological staining

The samples were stacked and placed into a 48-mm-diameter sample tube compatible with micro-computed tomography (micro-CT) for scanning. The scanning parameters were as follows: (i) voltage: 55 kVp; (ii) current: 145 pA; (iii) filter: Al 0.5 mm; (iv) exposure time: 250 ms; (v) scan resolution: 500 projections per 180°; and (vi) scan precision: 8 μm. The scanning data were used for 3D reconstruction using evaluation software (software, developer, country). Quantitative analysis of the subchondral bone volume fraction (BV/TV), bone mineral density (BMD), and trabecular bone number (Tb.N) was performed to assess the increase in subchondral bone.

2.5.3 Histological and morphological evaluation of regenerated osteochondral tissue

Samples were demineralized in a 10% ethylenediaminetetraacetic acid solution for 4 weeks. After dehydration and embedding in paraffin, demineralized samples were cut into 5-mm-thick sections. The sections were then subjected to hematoxylin and eosin staining and Safranin O staining to differentiate between newly formed cartilage and bone tissue. Additionally, immunohistochemical staining was performed to confirm the presence of type II collagen (COLII) in the newly formed cartilage tissue.

2.6 Statistical analysis

Data are presented as mean ± standard deviation. Differences between groups were analyzed using t-test and one-way analysis of variance, and $p < 0.05$ was considered statistically significant (software, developer, country).

3. Results

3.1. Scaffold morphological characterization

3.1.1. Scaffold microstructure

A bioplotter 3D printing system was employed to fabricate TDM/ZrO_2 hydrogel composite scaffolds. The incorporation of TDM particles enhanced print fidelity, resulting in more uniform and continuous filament extrusion. The printed constructs exhibited a milky-white and opaque appearance (Figure 2A), consistent with successful TDM integration. Compared to conventional hydroxyapatite-based scaffolds, the surfaces of the TDM/ZrO_2 scaffolds appeared notably rougher due to the irregular morphology of the TDM particles, which increased the effective surface area and was expected to facilitate cell attachment and adhesion (Figure S1). Demineralized TDM exhibited an extensive dentinal tubule network, facilitating the sustained release of embedded bioactive molecules into the surrounding matrix. This not only mitigated the partial occupation of GelMA domains by TDM particles but also contributed to the formation of a favorable biochemical microenvironment that promotes lineage-specific differentiation of stem cells involved in osteochondral regeneration.[26]

Internally, the scaffold architecture exhibited interconnected porous networks, which are critical for the diffusion of nutrients and oxygen, as well as the removal of metabolic waste products, thereby supporting cellular viability and activity. In the 0% TDM group, the absence of TDM led to significant structural collapse upon dehydration, with sparsely distributed ZrO_2 particles occupying the remaining voids (Figure 2B). In contrast, scaffolds with 30, 50, and 70% of TDM retained their macroscopic morphology following freeze-drying, suggesting improved dimensional stability and structural integrity. Side-view imaging demonstrated a clear layer-by-layer deposition pattern, characteristic of extrusion-based bioprinting (Figure 2C). Additionally, cross-sectional analysis revealed a loosely porous internal structure (Figure 2D), providing sufficient space for cell infiltration and proliferation and offering structural support for cell-laden bioprinting applications.

3.1.2. Physicochemical characterization of treated dentin matrix/zirconia hydrogel scaffolds

FTIR spectroscopy analysis confirmed that the major components of TDM closely resembled those of hydroxyapatite, containing characteristic organic functional groups such as carbonate and phosphate. Evidence of hydrogen-bonding interactions between GelMA and TDM was observed. In particular, the enhanced absorption peak at 1114 cm^{-1}, attributed to C–OH stretching vibrations and/or aliphatic C–N stretching, indicated the successful chemical integration of TDM into the composite scaffold (Figure 2E). The FTIR spectra of the 30, 50, and 70% TDM scaffolds exhibited similar peak patterns, with variations primarily in peak intensity and width corresponding to differences in TDM content. As the TDM concentration increased, the area of the characteristic peaks also increased, further supporting the dose-dependent integration of TDM into the scaffold matrix.

X-ray diffraction analysis provided additional insights into the phase composition of the scaffolds. In addition to the primary elements of hydroxyapatite (calcium, phosphorus, and carbon), the spectra also revealed the

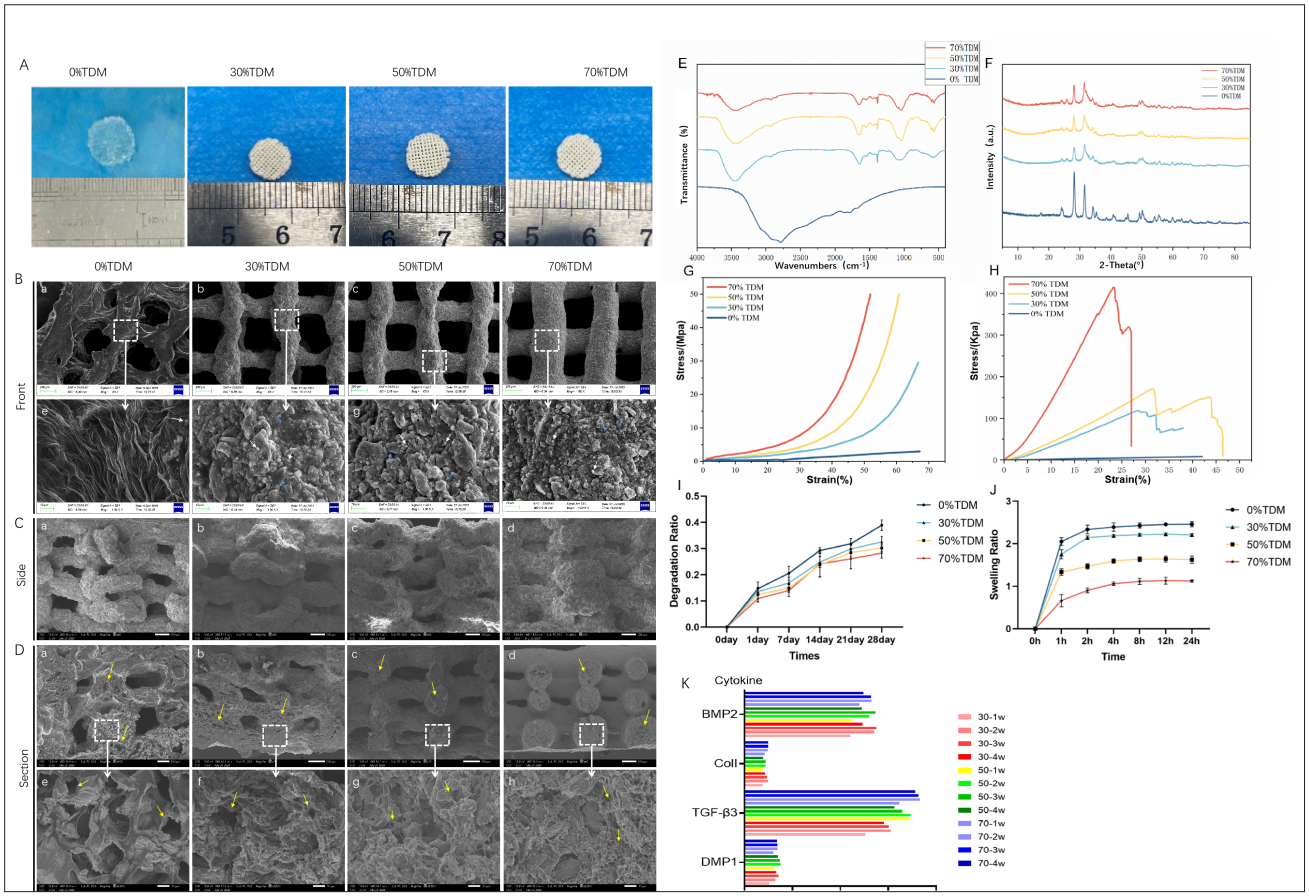

Figure 2. Morphological, structural, and mechanical characterization of 3D-printed TDM/ZrO_2 composite scaffolds. (A) 3D-printed composite scaffold used for various characterizations. (B) SEM images of the front views of 3D-printed scaffolds with different concentrations of TDM (scale bar: 200 μM; magnification: 60×). (C) SEM images of the TDM/ZrO_2 hydrogel scaffolds in side view (scale bar: 200 μM; magnification: 60×). (D) SEM images of the TDM/ZrO_2 hydrogel scaffolds in cross-sectional view, with yellow arrows indicating internal voids in the scaffold (scale bar: 100 μM; magnification: 200×). (E) Fourier transform infrared spectra of the scaffold material. (F) X-ray diffraction spectra of the scaffold material. (G, H) Stress–strain curves obtained from static compression and tensile tests and extrapolated Young's modulus. (I) Degradation ratio of 3D-printed scaffolds. (J) Swelling isotherms of 3D printed scaffolds. (K) Osteogenesis-associated protein released from scaffolds (n=4). Abbreviations: 3D, three-dimensional; SEM, scanning electron microscopy; TDM, treated dentin matrix; ZrO_2, zirconia.

presence of oxygen, magnesium, and sodium, along with trace amounts of nitrogen and sulfur, indicating the retention of both organic and mineral components from natural dentin. In the 0% TDM group, the diffraction pattern corresponded closely to the standard reference for ZrO_2 (PDF#88-1449), confirming its dominant phase composition. In contrast, scaffolds containing TDM exhibited diffraction peaks aligned with the hydroxyapatite reference pattern (PDF#73-0293), confirming the presence of both hydroxyapatite and ZrO_2 as the main crystalline phases. Notably, the broader full-width at half maximum of the TDM-related peaks suggested lower crystallinity in TDM compared to synthetic hydroxyapatite. Moreover, the gradual increase in the hydroxyapatite peak area across the 30, 50, and 70% TDM groups further supports the dose-dependent incorporation of TDM within the scaffold structure (Figure 2F).

3.1.3. Mechanical properties of three-dimensional printed scaffolds

The mechanical performance of the TDM/ZrO_2 scaffolds was evaluated under both compressive and tensile loading conditions. As the TDM content within the GelMA hydrogel matrix increased, the compressive strength of the scaffolds also increased. At 50% strain, the compressive strengths of the 30, 50, and 70% TDM groups reached 7.4, 22.5, and 48.2 MPa, respectively, with corresponding elastic moduli of 0.32, 0.65, and 0.89 MPa. These values fall within the range of native human cartilage and osteochondral composite structures (0.5–3 MPa and

5—54 MPa, respectively),[27] suggesting that the scaffolds exhibit mechanical properties physiologically relevant to native tissue. In contrast, the 0% TDM group exhibited a significantly lower compressive modulus of only 0.12 MPa (Figure 2G).

Tensile testing further confirmed the mechanical enhancement conferred by TDM incorporation. The tensile strengths of the 30, 50, and 70% TDM groups were 120, 150, and 342 kPa, respectively, compared to only 0.035 kPa in the 0% TDM group, which lacked the reinforcing TDM phase (Figure 2H). Collectively, both the compressive and tensile moduli were significantly improved in the gradient scaffolds relative to the pure hydrogel control, contributing to enhanced shape fidelity and defect conformity following *in vivo* implantation. This mechanical robustness provides a supportive and protective microenvironment for the proliferation and differentiation of the encapsulated seed cells during the early stages of tissue regeneration.

3.1.4. Degradation and swelling properties

The shape and structure of the scaffolds remained relatively stable during the first 2 weeks, showing no apparent structural damage or mass loss. After 21 days of incubation, the scaffolds maintained a relatively intact morphology. After 28 days of incubation, the 3D network structure gradually disintegrated and collapsed, accompanied by a significant increase in mass loss; however, the remaining mass still exceeded 70% of the initial weight. Beyond this point, the degradation profile reached a plateau, with only a gradual and slow decline in mass (Figure 2I). The 0% TDM group exhibited faster degradation and higher mass loss, attributed to the absence of mechanical reinforcement provided by TDM particles. As the TDM content increased, the degradation rate progressively decreased.

Both GelMA hydrogel and TDM particles possessed a porous structure and intrinsic water absorption capacity, which facilitate cell migration and nutrient transport, thereby supporting the survival of seeded cells within the printed scaffold. The freeze-dried scaffolds exhibited rapid water uptake and swelling behavior, with the mass reaching its peak at 6 h and gradually attaining swelling equilibrium at approximately 8 h (Figure 2J). As the TDM content increased, the SR of the scaffold decreased, as the GelMA network became progressively occupied by a greater number of TDM particles, which hindered the penetration and retention of water molecules.

3.1.5. Sustained release of osteogenic and chondrogenic factors from the scaffold

Owing to the porous structure of the scaffold and the encapsulation characteristics of the hydrogel, the scaffold continuously released osteogenic and chondrogenic proteins such as BMP2, TGF-β3, COL I, and DMP1, reaching a peak within 2–3 weeks. To more intuitively display the release profiles of these factors, a histogram was used. As the TDM content increased, the amount of released proteins also increased. Among them, TGF-β3 exhibited the highest concentration, reaching 363 ng/mL (Figure 2K). Compared with a previous study, in which TDM-related protein release primarily occurred within 1 week of culture,[24] the release of scaffold-related proteins in this study peaked at 2–3 weeks, demonstrating a significant sustained-release effect.

3.2. Biocompatibility of the scaffolds

The findings revealed that live cells were distributed in a grid-like arrangement along the scaffold morphology, whereas dead cells were scattered throughout the scaffolds (Figure 3A). To investigate the effect of the scaffold materials on cell viability, Cell Counting Kit-8 assays and live/dead staining were performed at various time points *in vitro*. Live/dead staining yielded consistent results, with only a few red fluorescent cells observed across all groups on days 5 and 7, showing no notable deviation from the control group (Figure 3B). The cell proliferation trends were similar between the scaffold co-culture and control groups. Over time, cells in all five groups continued to proliferate, leading to a gradual increase in the optical density values (Figure 3C). No significant differences were observed between the groups on corresponding days; however, significant differences were observed within each group ($p < 0.0001$). Notably, the optical density value of the control group on day 7 was comparable to that on day 5, possibly due to a slightly higher initial cell seeding density. By day 7 of culture, cells in the wells had reached over 90% confluency, indicating contact inhibition. These findings suggest that the TDM/ZrO_2 hydrogel scaffold material is non-toxic and does not hinder cell proliferation. Although the TDM/ZrO_2 hydrogel scaffold did not affect cell proliferation, it exhibited excellent biocompatibility, providing a solid foundation for subsequent *in vivo* experiments.

$SOX9^+$ precursor cells generally exhibited a spindle-shaped morphology within the scaffold, extending pseudopodia and displaying an elongated growth pattern (**Figure 3D**). The porous internal structure of the scaffold provided a favorable microenvironment for cell attachment and growth. After three days of *in vitro* culture of the cell-loaded printed scaffold, $SOX9^+$ precursor cells migrated outward from the scaffold surface (Figure 3E). The scaffolds in all groups demonstrated good biocompatibility with no evidence of significant cytotoxicity.

3.3. *In vitro* effects on cell biological behavior of treated dentin matrix/zirconia hydrogel scaffold

After co-culturing $SOX9^+$ scl-progenitors with TDM/ZrO_2 hydrogel scaffolds for seven days, the mRNA

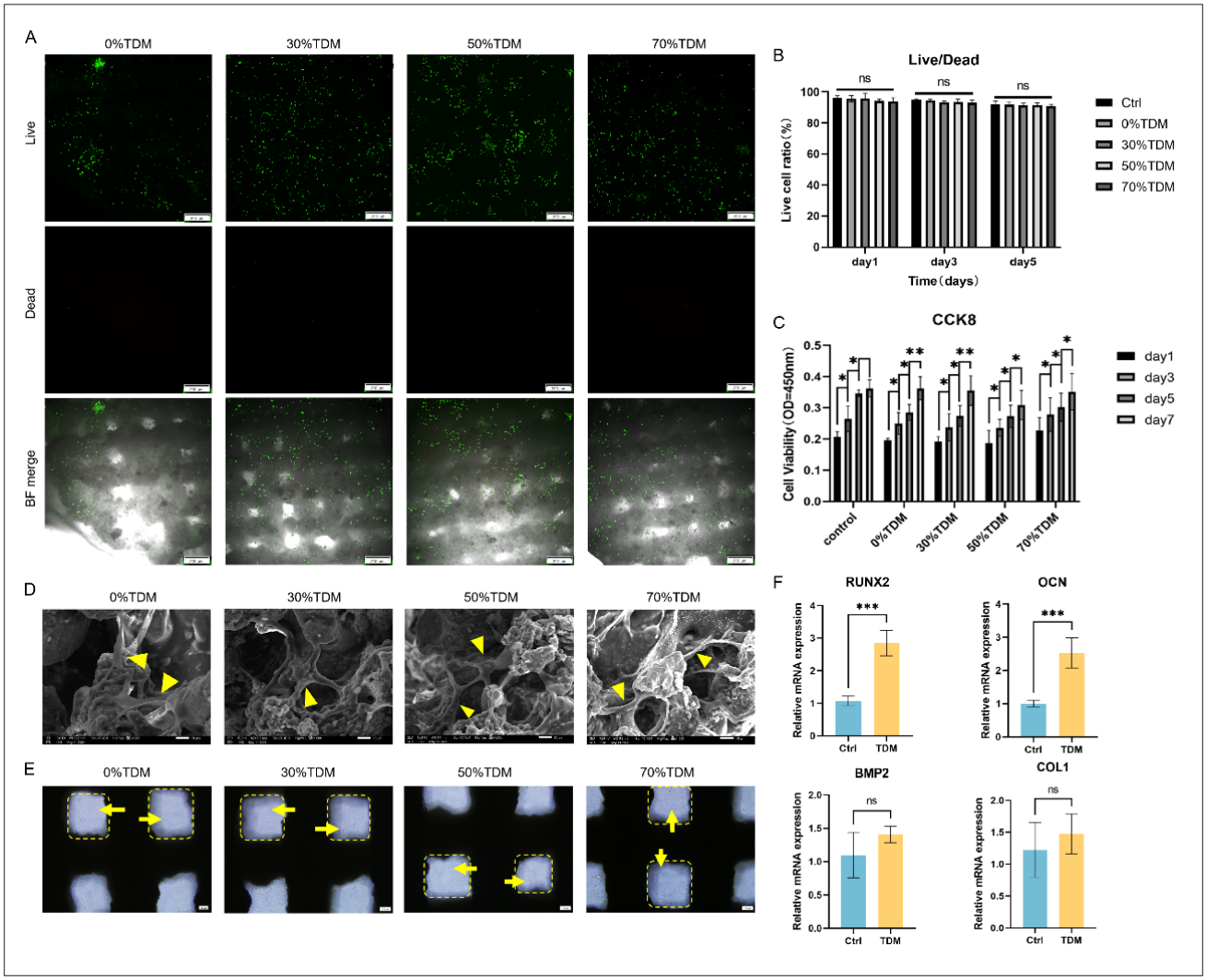

Figure 3. Biocompatibility and cell-scaffold interaction of the 3D-printed composite scaffold. (**A**) Viability of cells co-cultured with 3D-printed scaffolds for 4 days, assessed by Live/Dead staining (scale bar: 200 μm; magnification: 10×). (**B**) SEM image of a printed construct, with yellow arrows indicating cells extending pseudopodia on the scaffold surface (scale bar: 10 μm; magnification: 2000×). (**C**) Quantitative analysis of cell migration from the TDM/ZrO_2-GelMA scaffold over time. *, **, and *** indicate statistically significant differences at $p < 0.05$, $p < 0.01$, and $p < 0.001$, respectively. "ns" denotes no statistical significance. (**D**) SEM image of cellular growth within the scaffold, with a yellow arrow indicating a cell embedded in the internal structure (scale bar: 10 μm; magnification: 2000×). (**E**) Bright-field image showing cell migration, with a yellow arrow indicating a cell crawling out from the cell-laden printed scaffold (scale bar: 100 μm; magnification: 20×). (**F**) Gene expression levels of osteogenic and chondrogenic markers after 7 days of co-culture with the scaffolds.

expression levels of *OCN* and *RUNX2* were significantly higher than those of the control group, whereas the mRNA expression levels of *BMP2* and *COL1A1* showed no significant difference. The protein expression levels of OCN, RUNX2, and BMP2 were also increased (Figure 3F). RUNX2 is an important marker of late-stage chondrogenesis, and its upregulation can further promote the expression of the osteogenesis-related gene *OCN*. OCN is involved in bone formation and development, and is expressed in the early stages of osteogenesis.[28,29] These findings suggest that the TDM/ZrO2 hydrogel scaffold can promote the osteogenic and chondrogenic differentiation of SOX9⁺ scl-progenitors.

3.4. Transcriptomic changes in SOX9⁺ scl-progenitors following co-culture with the 50% TDM/ZrO_2 hydrogel scaffold

Comprehensive transcriptomic analysis of SOX9⁺ scl-progenitors cultured under standard conditions (control) and SOX9⁺ scl-progenitors co-cultured with the 50% TDM/ZrO_2 hydrogel scaffold was performed to characterize RNA expression profiles. As shown in Figure 4A, 162 genes were upregulated and 141 genes were downregulated

in the TDM group compared with the control group. Differentially expressed genes were analyzed using Gene Ontology, a bioinformatics approach encompassing three main categories (Figure 5B). Notably, the analysis revealed that genes related to extracellular matrix organization ($p < 0.001$) and encapsulating structure formation ($p < 0.005$) were significantly upregulated, indicating alterations in organelle-associated processes, particularly those involving membrane-bound organelles (Figure 4C).

Kyoto Encyclopedia of Genes and Genomes (KEGG) pathway enrichment analysis was conducted to identify potential signaling pathways through which TDM may regulate bone tissue regeneration. The calcium signaling pathway, known to modulate osteoblastic differentiation and bone formation,[30] was significantly upregulated. Notably, the hypoxia-inducible factor 1 signaling pathway, which plays a critical role in maintaining bone homeostasis and regulating glycolytic metabolism in chondrocytes, was also significantly enriched among the differentially expressed genes,[31,32] indicating its potential involvement in scaffold-induced cellular responses (Figure 4D).

To further validate the transcriptomic results and assess gene expression during the chondrogenic and osteogenic differentiation of SOX9$^+$ scl-progenitors, quantitative reverse transcription PCR was performed after seven days of co-culture. The TDM group exhibited significantly increased expression of *VEGFA*, *SOX9*, *GLUT1*, *COL2A1*, and *CDC6*, whereas *MMP7* and *KLF15* were downregulated (Figure 4E).

Western blot analysis revealed consistent trends, except that SOX9 protein expression showed no significant difference (Figure 4F), which may be attributed to the duration of the culture period. Similarly, the cell spheroids demonstrated robust glycosaminoglycan deposition, sustained chondrogenic differentiation, and abundant expression of COL2A1 (Figure S4).

These findings suggest that the TDM/ZrO_2 hydrogel scaffold promotes cell proliferation and angiogenesis while suppressing the expression of matrix metalloproteinases (MMPs), which are associated with osteoarthritis and articular cartilage degeneration.[33] Furthermore, it enhances the osteogenic and chondrogenic differentiation of SOX9$^+$ scl-progenitors, thereby supporting osteochondral tissue regeneration.

3.5. Calcification and hypertrophy following subcutaneous implantation

Under 3D culture conditions, SOX9$^+$ scl-progenitors spontaneously aggregated into compact spheroids with well-defined spherical shapes and smooth surfaces. Microscopic observation revealed that the spheroids exhibited a densely packed structure with strong cell–cell adhesion. The cell surfaces exhibited abundant microvilli-like protrusions, indicating high cellular activity and enhanced intercellular interactions, which collectively provided a favorable microenvironment for subsequent differentiation and tissue regeneration (Figure S3). After subcutaneous implantation of TDM/ZrO_2 hydrogel-encapsulated cell spheroids (Figure 5A), cells in all four groups exhibited robust chondrogenic differentiation by week 4, with no evidence of calcification or hypertrophy.

Higher magnification images revealed cells residing within cartilage lacunae, whereas darkly stained granules at the edges represented the printed material (Figure 5B). By week 8, Alcian blue staining showed that the cell nuclei were light blue, and the cytoplasm contained abundant glycosaminoglycans (Figure 5C). In the 0% TDM group, cells did not exhibit calcification or hypertrophy, whereas in the 30, 50, and 70% TDM groups, significant calcification and hypertrophy were observed. At this stage, the cells secreted more cartilage matrix, adopted a moderately cuboidal morphology, and were noticeably larger than the surrounding cells. Furthermore, Alizarin red staining demonstrated distinct calcified nodules within the cell spheroids, with some cells differentiating toward the osteogenic lineage (Figure 5D). Importantly, at both week 4 and week 8, no teratoma formation or tumorigenic cells were detected in any of the subcutaneous implants.

Fluorescein isothiocyanate labeling confirmed the presence of type X collagen (ColX)-positive chondrocytes, indicating chondrocyte hypertrophy, which is a hallmark of chondrocyte maturation. In the 30, 50, and 70% TDM groups, ColX expression overlapped with the calcified regions identified by Alizarin red staining (Figure 5E). These ColX-positive cells exhibited an enlarged cellular volume compared with surrounding cells and produced higher levels of ColX, while the production of COL2A1 decreased, indicating the initiation of osteogenic differentiation.[34–36]

3.6. *In vivo* osteochondral regeneration by SOX9$^+$ cell scaffolds

The results of hematoxylin and eosin staining of organs harvested from nude rats at weeks 6 and 12 are provided in the Supplementary file. No significant abnormalities were observed in any group (Figure S5). Based on the gross images (Figure S6), a significant concavity remained at the defect site at week 6, with the blank control group exhibiting the most pronounced depression. In contrast, the 70% TDM group exhibited a relatively smoother surface at the defect site. The micro-CT reconstructed model of the nude rat knee joint provided a more intuitive visualization of the bone tissue defect repair process. By week 12, the defect sites in the scaffold-implanted groups

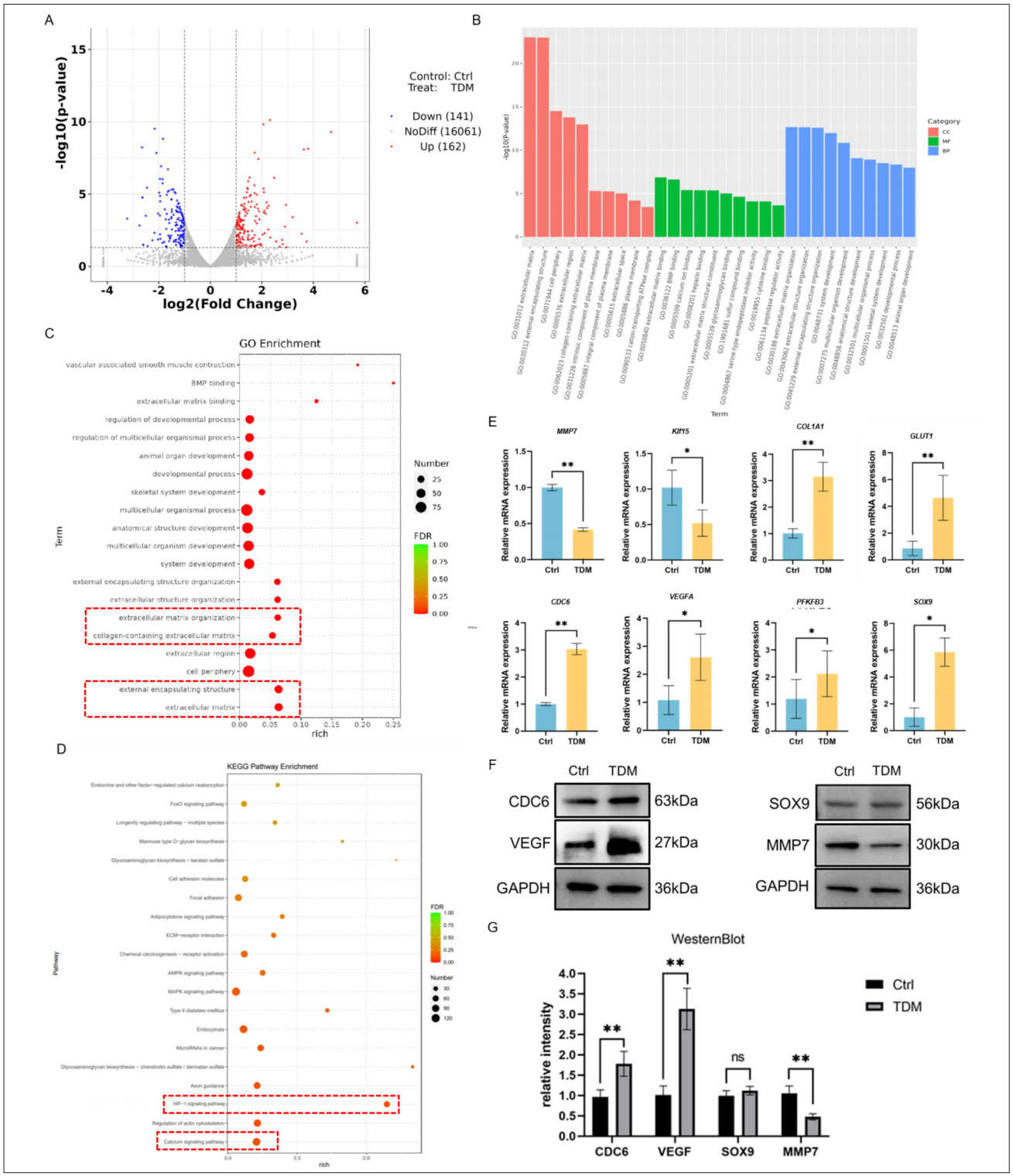

Figure 4. Transcriptome profiling and validation of differentially expressed genes in TDM-treated sclerotomal progenitors. (A) Significantly upregulated and downregulated genes in the TDM versus the control groups. (B) Differentially expressed genes classified by GO. (C) GO enrichment of upregulated genes in the TDM groups compared with the control group. (D) KEGG pathway enrichment of differentially expressed genes, depicting up- and downregulated RNAs. (E) mRNA expression of selected differentially expressed genes of SOX9^{+} sclerotomal progenitors. (F) Protein expression of selected differentially expressed genes. (G) Quantitative analysis of Western blot results. * and ** indicate statistically significant differences at $p < 0.05$ and $p < 0.01$, respectively. "ns" denotes no statistical significance. Abbreviations: Ctrl, control; GO, gene oncology; KEGG: Kyoto Encyclopedia of Genes and Genomes; TDM, treated dentin matrix.

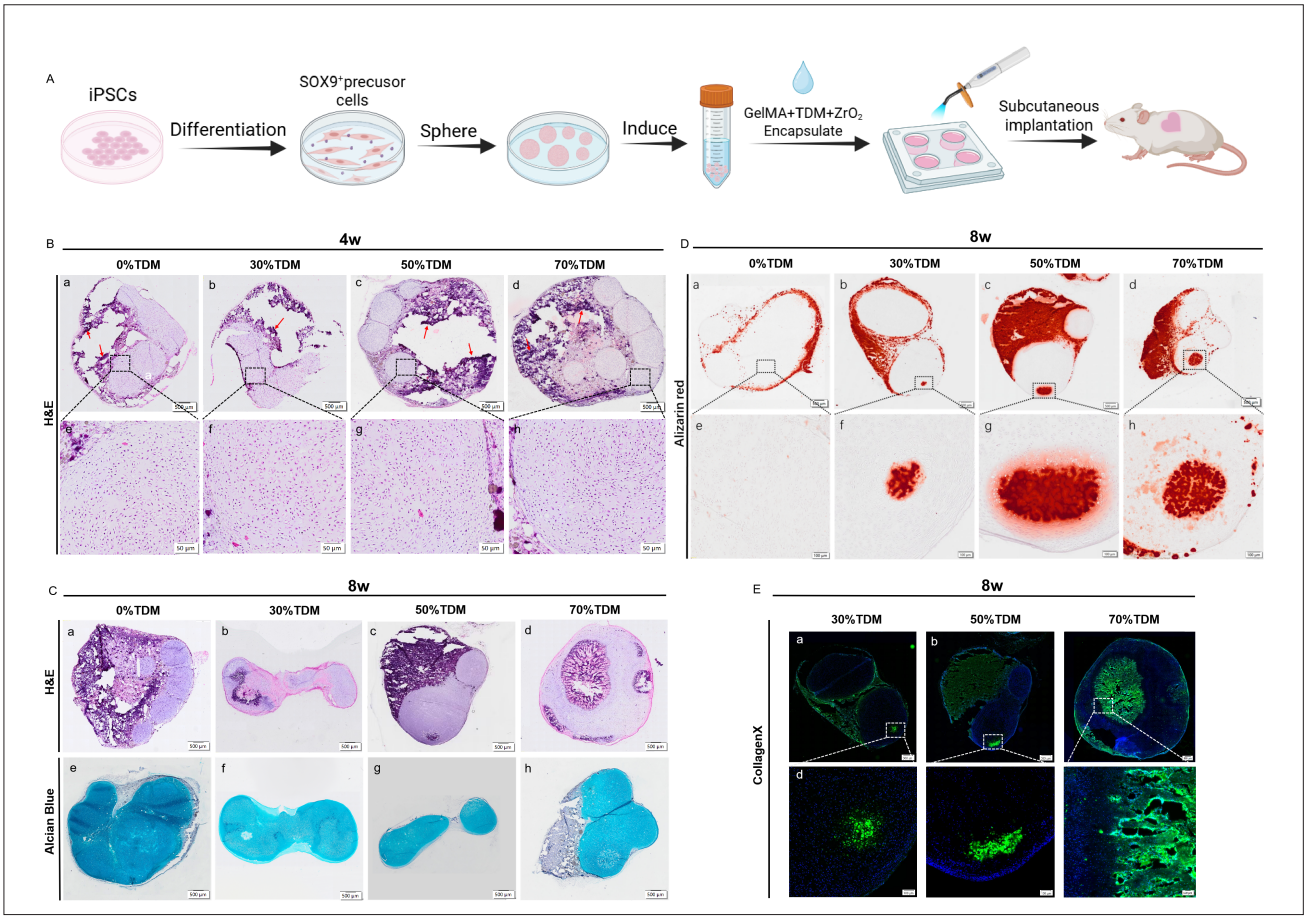

Figure 5. In vivo implantation of SOX9+ sclerotomal progenitor spheroids in 3D-printed scaffolds and subsequent evaluation of tissue formation and osteochondral differentiation. (A) Schematic diagram of subcutaneous implantation of SOX9⁺ sclerotomal progenitor spheroids encapsulated in three-dimensional-printed scaffolds. (B) H&E staining at week 4 after subcutaneous implantation, with red arrows indicating the 3D-printed scaffolds (scale bar: 500 μM; magnification: 10×). (C–E) Histological and immunofluorescence analysis at week 8: (C) H&E and Alcian blue staining (scale bar: 500 μM; magnification: 10×), (D) Alizanin red staining (scale bar: 500 μM; magnification: 10×), and (E) type X collagen immunofluorescence staining (scale bar: 500 μM; magnification: 10×). Abbreviations: GelMA, methacrylated gelatin; H&E, hematoxylin and eosin; iPSC, induced pluripotent stem cell; TDM, treated dentin matrix; ZrO_2, zirconia.

were no longer easily distinguishable from the surrounding tissue. An increase in TDM content within the scaffold correlated with a more pronounced repair of the defect site (Figure 6A). A semi-transparent, cartilage-like layer covered the center of the trochlear region, with faint reddish hard tissue visible beneath (Figure 6B). However, a distinct concavity persisted in the blank control group.

Micro-CT analysis quantified the BMD (g/cm^3), BV/TV (%), and Tb.N (mm^{-1}) in samples collected at weeks 6 and 12, with the corresponding statistical results shown in Figure 6. The blank control group at week 6 exhibited the lowest BMD and Tb.N values, with statistically significant differences compared with other groups (Figure 6C). However, the difference between the blank control and 0% TDM groups was not statistically significant. This may be attributed to the fact that SOX9⁺ scl-progenitors primarily contribute to cartilage repair, whereas bone repair predominantly relies on TDM within the scaffold material. As the TDM content increased, BMD showed a gradual increase, with the TDM scaffold-implanted group exhibiting an average of approximately 70% in both BMD and Tb.N. On average, bone tissue repair was significantly improved, and BV/TV was significantly increased (Figure 6D). Although the average Tb.N in the 30% TDM group was higher than that in the 0% TDM group, the difference was not statistically significant (Figure 6E), suggesting that TDM concentration plays a crucial role in bone mass recovery.

Macroscopic cartilage repair in each group was further evaluated using the cartilage injury grading system proposed by the International Cartilage Repair Society.[37] The scoring results are shown in Figure 6F. At week 6,

although the 0% TDM group had a higher average score than the control group, the difference was not statistically significant. However, by week 12, a statistically significant difference was observed between the two groups (Figure 6F). TDM groups exhibited significantly higher scores than the control group. Notably, the 70% TDM group achieved average scores of 10.9 and 13.67 at weeks 6 and 12, respectively, while the 50% TDM group reached a score of 11.1 at week 12, corresponding to Grade II (nearly normal) in the cartilage injury grading system.

These findings indicate that the TDM/ZrO_2 hydrogel scaffold loaded with SOX9$^+$ scl-progenitors possesses strong therapeutic potential for osteochondral defect repair. The synergistic interaction between TDM and SOX9$^+$ scl-progenitors significantly enhanced the repair process, leading to superior tissue regeneration compared with scaffolds lacking TDM-loaded cells.

3.7. Histological assessment of scaffold-mediated osteochondral repair

Safranin-fast green staining results indicated that no significant subchondral bone repair was observed in either the control or 0% TDM group at week 6. The control group exhibited extensive fibrous proliferation, whereas the 0% TDM group displayed a notable depression at the defect site (Figure 6G). As the quality of the scaffold material improved, degradation resulted in gaps within the tissue; however, the 30, 50, and 70% TDM groups demonstrated substantial cartilage repair, active subchondral bone trabecular proliferation, and smooth joint surfaces.

After 12 weeks, the control group still exhibited pronounced surface defects, while the 0% TDM group retained a greater amount of cartilage-like tissue. The 30% TDM group exhibited less cartilage tissue than the 0% TDM group but greater subchondral bone repair, whereas the 50% TDM group exhibited more cartilage tissue than the 0% TDM group. The 50% TDM and 70% TDM groups, containing higher levels of TDM, induced hypertrophy and maturation of SOX9$^+$ precursor cells, leaving only a layer of collagen fibers on the surface of the newly formed bone (Figure 6H). COL2A1 expression was most pronounced in the 0 and 30% TDM groups (Figure S7). In contrast, COLII expression in the 50% TDM and 70% TDM groups was relatively lower, although still higher than that in the control group. This may be attributed to the increased TDM content, particularly its hydroxyapatite component, which accelerates cartilage hypertrophy and calcification, thereby promoting enhanced osteogenic differentiation. Implantation of the cell-loaded scaffold did not cause any significant systemic effects in the nude rats (Figure S5).

4. Discussion

Articular cartilage is composed of a three-layer gradient structure, comprising hyaline cartilage, calcified cartilage, and subchondral bone.[38,39] Collagen fibers run perpendicular to the joint surface, traverse the calcified layer, and anchor into the subchondral bone.[40,41] This osteochondral interface, consisting of the tidemark, calcified cartilage, and subchondral bone plate, functions as a structurally and biologically complex composite that is essential for load transmission and joint integrity.[42,43]

Osteochondral injuries can be classified as partial-thickness cartilage lesions, full-thickness defects, and injuries involving the subchondral bone.[44] A hallmark of osteochondral defects is the damage to the subchondral bone plate.[9] Associated pathological features, such as sclerosis, osteophyte formation, and bone remodeling, are common in conditions such as osteoarthritis and can significantly affect treatment outcomes.[10] Existing clinical strategies, including arthroscopic debridement, microfracture, and abrasion arthroplasty, often lead to the formation of fibrous cartilage, which lacks the mechanical and biochemical properties of native hyaline cartilage.[7] Autologous chondrocyte implantation, considered the current gold standard, is hindered by limited cell availability, donor site morbidity, and the need for additional surgery.[45] Therefore, there is a pressing need for regenerative strategies that can promote both chondrogenesis and osteogenesis within a single construct.

In this context, the selection of appropriate seed cells is vital for successful osteochondral regeneration. Among common candidates, MSCs are widely used but often exhibit undesired ossification and vascularization *in vivo*.[46] Embryonic stem cells possess strong regenerative capacity but face ethical and safety concerns. In contrast, iPSCs combine embryonic stem cell-like pluripotency with improved accessibility and immunocompatibility.[47,48]

In this study, we employed genetic reprogramming to induce high levels of SOX9 expression, a master transcription factor for chondrogenesis, in iPSCs. The resulting SOX9$^+$ scl-progenitors exhibited downregulated expression of pluripotency markers (*OCT4* and *NANOG*) and upregulated expression of differentiation markers (*SOX9* and *TWIST1*), indicating a stable commitment to the chondrogenic or osteogenic lineage. These cells were sorted via tdTomato fluorescence labeling and flow cytometry to obtain a high-purity population (>99.6%). Notably, SOX9 serves as a central integrator of chondrogenic signaling pathways and regulates key processes in cartilage formation and maintenance.[49,50]

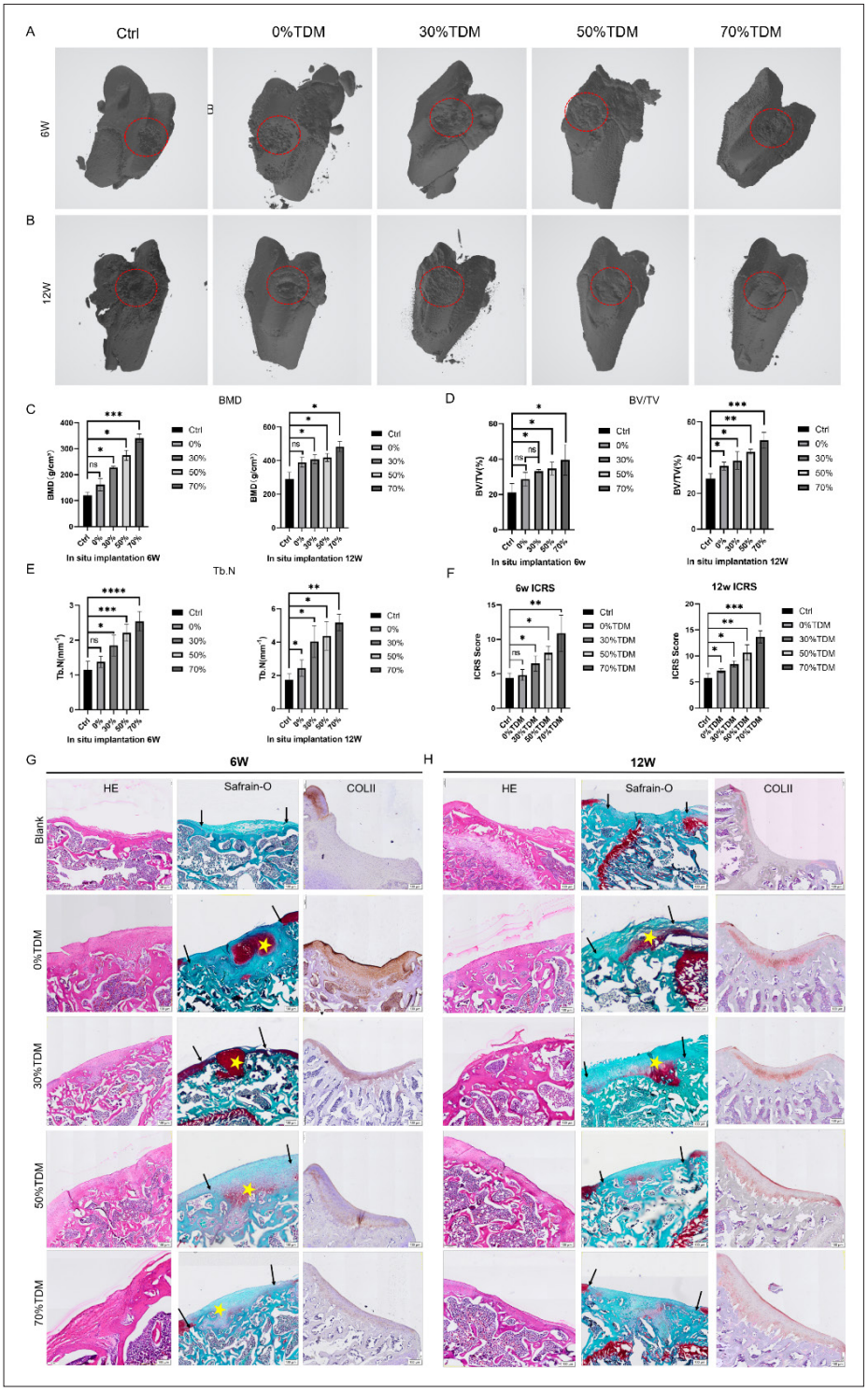

Figure 6. In vivo evaluation of osteochondral defect repair using 3D-printed scaffolds with varying TDM concentrations. (A, B) Micro-computed tomography reconstructed images at (A) week 6 and (B) week 12. (C) BMD at the defect site. (D) BV/TV. (E) Tb.N (n=3). (F) Cartilage damage assessed using the ICRS score. (G, H) H&E staining, Safranin O staining, and COLII immunohistochemistry of knee joint implantation at (G) week 6 and (H) week 12. Groups included blank, 0, 30, 50, and 70% TDM scaffold implantation. Arrows indicate scaffold placement, and stars indicate red-stained cartilage tissue (scale bar: 200 μM; magnification: 10×). *, **, and *** indicate statistically significant differences at $p < 0.05$, $p < 0.01$, and $p < 0.001$, respectively. "ns" denotes no statistical significance. Abbreviations: BMD, bone mineral density; BV/TV, bone volume fraction; COLII, type II collagen; Ctrl, control; H&E, hematoxylin and eosin; ICRS: International Cartilage Research Society; Tb.N, trabecular bone number; TDM, treated dentin matrix.

The need for personalized, mechanically robust, and biologically active scaffolds to match these cell sources has driven the development of 3D-printed biomaterial systems. Tissue engineering approaches offer promising potential, enabling the fabrication of customized, biomimetic scaffolds with precise architectures tailored to individual anatomical and functional needs.[51,52] Within this framework, TDM has emerged as a promising scaffold component. As a natural decellularized extracellular matrix, TDM retains bioactive molecules such as low-crystallinity hydroxyapatite, collagen type I, TGF-β, and BMP-2. These components have been shown to enhance the proliferation and osteogenic or odontogenic differentiation of various types of stem cells. Our previous studies demonstrated that TDM/polycaprolactone scaffolds exhibit superior mechanical properties compared with HA/polycaprolactone scaffolds, with an elastic modulus similar to that of demineralized dentin. Moreover, TDM scaffolds maintained their structural integrity over six months *in vivo*, with only a minor reduction in mechanical strength, whereas the HA group showed a marked decline.[19]

Importantly, TDM exhibits concentration-dependent biological effects: low concentrations favor cell proliferation, whereas higher concentrations promote osteogenic differentiation.[13] This dual functionality allows for the precise tuning of scaffold bioactivity according to regenerative needs. The incorporation of TDM into GelMA hydrogels significantly improves the mechanical strength of the scaffold, while the addition of nano-ZrO_2 helps to fill internal pores, thereby enhancing durability, drug resistance, and structural stability under cyclic mechanical stress.[53] Microscopic characterization confirmed the high porosity of the scaffold, which supports cell adhesion and infiltration, and *in vitro* biocompatibility assays demonstrated that the scaffold did not impair cell proliferation. Additionally, *in vivo* toxicity assessments showed no evidence of organ damage or systemic toxicity, confirming the biosafety of ZrO_2 at the applied dose and implantation method.[54]

Previous studies have emphasized that the compressive modulus of native articular cartilage varies substantially depending on the anatomical site, tissue depth, and testing methodology. Eschweiler *et al.*[55] reported aggregate moduli ranging from 0.5 to 0.9 MPa in healthy human cartilage, while more recent studies have extended this range up to 3.0 MPa, highlighting inter-study variability.[56] As a composite tissue, the osteochondral unit exhibits higher stiffness, with compressive moduli of approximately 5–54 MPa depending on site-specific and methodological differences.[57] These gradients reflect the hierarchical structure of the cartilage—from the softer superficial zone to the stiffer deep zone and subchondral bone—which collectively provide both shock absorption and load-bearing capacity. Within this context, the compressive moduli achieved by our scaffolds (0.32–0.89 MPa) are consistent with the native cartilage range, while the compressive strengths (7.4–48.2 MPa) overlap with those of the osteochondral unit. This dual-level correspondence suggests that the TDM/ZrO_2 scaffolds not only mimic the mechanical behavior of cartilage but also approximate the structural robustness of osteochondral composites, thereby offering the mechanical resilience necessary for load-bearing joint environments.

In this study, spheroids of SOX9$^+$ scl-progenitors were encapsulated within TDM/ZrO_2 hydrogel bioinks and implanted subcutaneously in immunodeficient mice. This *in vivo* model facilitated the evaluation of the biological behavior and regenerative potential of the combined cell–scaffold system. Transcriptome sequencing validated our hypothesis: the TDM/ZrO_2 scaffold significantly enhanced the osteochondral repair capacity of SOX9$^+$ scl-progenitors. Among the 303 differentially expressed genes, a marked downregulation of *MMP* family members was observed, particularly *MMP7*, a key enzyme involved in the degradation of COLII and the pathogenesis of osteoarthritis.[58] Conversely, *CDC6*—a gene involved in DNA replication and cell cycle progression—was significantly upregulated, indicating active cell proliferation.[59,60] The expression of *VEGFA* was also elevated, suggesting enhanced angiogenic potential, which is critical for effective bone tissue regeneration.[61,62]

After co-culturing SOX9$^+$ scl-progenitors with TDM/ZrO_2 hydrogel scaffolds for seven days, the mRNA expression levels of *OCN* and *RUNX2* were significantly higher than those of the control group, whereas the mRNA expression levels of *BMP2* and *COL1A1* demonstrated no significant difference. *BMP2* has been reported to promote SOX9-driven chondrogenesis and cartilage tissue formation, although it can also induce ossification under certain conditions.[63,64] Several studies have reported that *RUNX2* is closely associated with chondrocyte hypertrophy and osteogenic differentiation, and its upregulation may reflect a shift toward hypertrophy and endochondral ossification rather than stable cartilage formation.[65,66]

Notably, we observed an inconsistency between *SOX9* mRNA upregulation and the lack of significant changes in SOX9 protein expression, consistent with previous studies in stem cell differentiation contexts, where transcriptional activation of *SOX9* does not immediately translate into detectable protein accumulation.[67] Possible explanations include post-transcriptional regulation by microRNAs,

translational delays, or rapid protein turnover.[68] In addition, the culture duration in our study may not have been sufficient for protein levels to reach a detectable threshold. While our findings highlight the importance of *SOX9* in regulating chondrogenic differentiation, we acknowledge that the mRNA–protein discrepancy warrants further investigation. Future studies should focus on time-course analyses and mechanistic validation to better elucidate the regulatory dynamics of *SOX9* expression.

Our RNA sequencing results revealed significant enrichment of the hypoxia-inducible factor 1 signaling pathway, which is consistent with its known role in regulating chondrocyte survival and matrix metabolism under hypoxic conditions.[69] While this finding is intriguing, it remains to be clarified whether the observed activation is specifically elicited by the bioactive components of TDM or reflects the hypoxic microenvironment characteristic of dense 3D cell-laden scaffolds.

These transcriptomic findings were further supported by the *in vivo* implantation analysis. The cell-laden scaffolds showed no signs of systemic toxicity; histological analysis revealed no morphological abnormalities in the spleen, liver, or kidney; and blood biochemical parameters remained within normal ranges. Moreover, histological staining demonstrated hyaline cartilage regeneration in groups with lower TDM content (0 and 30%), whereas higher TDM levels (50 and 70%) favored osteogenic differentiation, likely due to the hydroxyapatite-rich composition of TDM. Safranin O/fast green staining confirmed the presence of cartilage, bone, and fibrous tissue within the repair site, reflecting distinct stages of endochondral ossification.

In a fully developed joint, the zonal architecture comprises fibrous, proliferative, mature, and hypertrophic layers, which are critical for mechanical and biological functions. During endochondral ossification, *SOX9* expression sharply declines in the hypertrophic zone, marking the transition toward bone formation. Thus, the precise modulation of TDM content may offer a strategy to recreate this native zonal structure and direct tissue-specific differentiation. The presence of COLII in the regenerated cartilage indicates the production of hyaline cartilage, reflecting the functional integrity of the cartilage tissue.[10] Safranin O/fast green staining effectively distinguished cartilage, bone, and fibrous tissue. In the control group, the defect was predominantly filled with dense fibrous tissue. Conversely, the 0 and 30% TDM groups exhibited repair of cartilage-like tissues. In the 50 and 70% TDM groups, where the primary component of TDM is hydroxyapatite, cell differentiation and maturation were enhanced.[70] Consequently, the defect was primarily repaired by bone and fibrous tissues, which accounts for the discrepancies observed in the staining results among the samples and sections. Our findings suggest that by adjusting the scaffold composition and integrating iPSC-derived SOX9$^+$ scl-progenitors, it is possible to guide the regeneration of functional osteochondral tissue.

Previous studies have established that iPSC-derived SOX9$^+$ scl-progenitors are not restricted to a single lineage fate, but instead display bipotent differentiation potential that mirrors the endochondral ossification process.[12] These cells can first generate cartilaginous templates and subsequently contribute to bone formation, mimicking the developmental programs of skeletal tissue morphogenesis. In the context of our osteochondral scaffold system, such lineage flexibility provides a developmental rationale for their capacity to support both chondral and subchondral bone regeneration within the defect site.

A limitation of the present study is the absence of a gradient-based or zone-specific scaffold design that more closely mimics the native cartilage-to-bone transition. Gradient or multiphasic scaffolds have been widely recognized as advantageous for osteochondral repair, as they enable smooth compositional and mechanical transitions that promote interface integration and zonal tissue formation.[71] Recent studies have demonstrated that gradient or multiphasic scaffolds fabricated via 3D printing can better replicate the osteochondral interface, thereby enhancing integration and zonal tissue formation.[72,73] In contrast to these gradient strategies, our current design served as a simplified proof-of-concept model to validate the feasibility of the TDM/ZrO_2 bioink with SOX9$^+$ progenitors. Future studies should focus on implementing layer-by-layer or continuous gradient printing (e.g., varying TDM/ZrO_2 ratios, graded crosslinking, and zonal growth factor delivery) to recreate the osteochondral gradient and evaluate both interface mechanics and long-term functional outcomes.

Advances in biomaterial design and nanotechnology will continue to improve scaffold efficacy and drive innovations in iPSC-based osteochondral tissue engineering. Additionally, a deeper understanding of the signaling mechanisms that regulate the differentiation of iPSC-derived SOX9$^+$ scl-progenitors remains a key objective in translating these findings into clinical application.

5. Conclusion

This study presents a customizable 3D-bioprinted scaffold system that leverages the developmental potential of iPSC-derived SOX9$^+$ scl-progenitors and the biological

and mechanical advantages of TDM/ZrO_2 composites. The scaffolds exhibited excellent mechanical properties, biocompatibility, and bioactivity, while the $SOX9^+$ scl-progenitors demonstrated stable chondrogenic potential and favorable *in vivo* outcomes. Future work should focus on fine-tuning TDM concentrations to engineer layered osteochondral structures, as well as elucidating the molecular signaling mechanisms governing SOX9-mediated lineage commitment. These advancements will help facilitate the translation of this approach toward clinically applicable regenerative therapies for joint cartilage and subchondral bone defects.

Acknowledgments

We appreciate the technical assistance provided by the laboratory staff for the experimental procedures

Funding

This work was supported by grants from the National Nature Science Foundation of China (82270958), the Major Science and Technology Projects in Yunnan Province(202302AA310038), and West China Hospital of Stomatology, Sichuan University Interdisciplinary innovation projects with research and development projects (RD-03-202106).

Conflict of interest

The authors declare that they have no affiliations with or involvement in any organization or entity with any financial interest in the subject matter or materials discussed in this manuscript.

Author contributions

Conceptualization: Weihua Guo, Yuqing Dong
Data curation: Jingfei Xiong, Fengxiao Zhao
Formal analysis: Yuqing Dong, Weihua Guo
Investigation: Jingfei Xiong, Fengxiao Zhao
Project administration: Weihua Guo, Zhonghan Li
Resources: Zhijun Zhang
Writing–original draft: All authors
Writing–review & editing: Yuqing Dong, Yuming Zhao
All authors have read and approved the final manuscript.

Ethics approval and consent to participate

All experimental procedures were approved by the Institutional Animal Care and Use Committee of West China Hospital (ethics approval number: WCHSIRB-D-2023-309) and complied with the National Institutes of Health guidelines for the care and use of laboratory animals.

Consent for publication

Not applicable.

Availability of data

All data associated with this study are presented in the paper.

References

1. Everhart JS, Abouljoud MM, Flanigan DC. Role of full-thickness cartilage defects in knee osteoarthritis (OA) incidence and progression: data from the OA initiative. *J Orthop Res*. 2019;37(1):77-83.
doi: 10.1002/jor.24140

2. Lee WY-w, Bin W. Cartilage repair by mesenchymal stem cells: clinical trial update and perspectives. *J Orthop Transl*. 2017;9:76-88.
doi: 10.1016/j.jot.2017.03.005

3. Shi W, Sun M, Hu X, *et al*. Structurally and functionally optimized silk-fibroin gelatin scaffold using 3D printing. *Adv Mater*. 2017;29(29).
doi: 10.1002/adma.201701089

4. Levingstone TJ, Moran C, Almeida HV, Kelly DJ, O'Brien FJ. Layer-specific stem cell differentiation in trilayered tissue engineering biomaterials: towards development of a single-stage cell-based approach for osteochondral defect repair. *Mater Today Bio*. 2021;12.
doi: 10.1016/j.mtbio.2021.100173

5. Minnig MCC, Golightly YM, Nelson AE. Epidemiology of osteoarthritis_ literature update 2022–2023. *Curr Opin Rheumatol*. 2024;36(2):108-112.
doi: 10.1097/BOR.0000000000000985

6. Tang H, Zhu W, Cao L, *et al*. miR-210-3p protects against osteoarthritis through inhibiting subchondral angiogenesis by targeting the expression of TGFBR1 and ID4. *Front Immunol*. 2022;13.
doi: 10.3389/fimmu.2022.982278

7. Jiang L, Zhou X, Xu K, *et al*. miR-7_EGFR_MEGF9 axis regulates cartilage degradation in osteoarthritis via PI3K_AKT_mTOR signaling pathway. *Bioengineered*. 2021;12(1):8622-8634.
doi: 10.1080/21655979.2021.1988362

8. Costa E, Gonzalez-Garcia C, Gomez Ribelles JL, Salmeron-Sanchez M. Maintenance of chondrocyte phenotype during expansion on PLLA microtopographies. *J Tissue Eng*. 2018;9:2041731418789829.
doi: 10.1177/2041731418789829

9. Kovács B, Vajda E, Nagy EE. Regulatory effects and interactions of the Wnt and OPG-RANKL-RANK signaling at the bone-cartilage interface in osteoarthritis. *Int J Mol Sci*. 2019;20(18).
doi: 10.3390/ijms20184653

10. Hsieh Y-H, Shen B-Y, Wang Y-H, Lin B, Lee H-M, Hsieh M-F. Healing of osteochondral defects implanted with biomimetic scaffolds of poly(ε-caprolactone)_hydroxyapatite and glycidyl-methacrylate-modified hyaluronic acid in a Minipig. *Int J Mol Sci*. 2018;19(4);1125. doi: 10.3390/ijms19041125

11. Liao Y, Kang F, Xiong J, *et al*. MSX1(+)PDGFRA(low) limb mesenchyme-like cells as an efficient stem cell source for human cartilage regeneration. *Stem Cell Reports*. 2024;19(3):399-413. doi: 10.1016/j.stemcr.2024.02.001

12. Xiong J, Ma R, Xie K, *et al*. Recapitulation of endochondral ossification by hPSC-derived SOX9+ sclerotomal progenitors. *Nat Commun*. 2025;16(1):2781. doi: 10.1038/s41467-025-58122-9

13. Chen G Chen J, Yang B, *et al*. Combination of aligned PLGA gelatin electrospun sheets, native dental pulp extracellular matrix and treated dentin matrix as substrates for tooth root regeneration. *Biomaterials*. 2015;52:56-70. doi: 10.1016/j.biomaterials.2015.02.011

14. Grawish ME, Grawish LM, Grawish HM, *et al*. Demineralized dentin matrix for dental and alveolar bone tissues regeneration: an innovative scope review. *Tissue Eng Regen Med*. 2022;19(4):687-701. doi: 10.1007/s13770-022-00438-4

15. Li M, Yang S, Song J, *et al*. Different grinding speeds affect induced regeneration capacity of human treated dentin. *J Biomed Mater Res*. 2021;110(4):755-767. doi: 10.1002/jbm.b.34954

16. Wen B, Dai Y, Han X, *et al*. Biomineralization-inspired mineralized hydrogel promotes the__repair and regeneration of dentin_bone hard tissue. *NPJ Regen Med*. 2023;8(1):253-262. doi: 10.1038/s41536-023-00286-3

17. Wen B, Huang Y, Qiu T, *et al*. Reparative dentin formation by dentin matrix proteins and small extracellular vesicles. *J Endod*. 2021;47(2):253-262. doi: 10.1016/j.joen.2020.11.017

18. Chen J, Cui C, Qiao X, *et al*. Treated dentin matrix paste as a novel pulp capping agent for dentin regeneration. *J Tissue Eng Regen Med*. 2017;11(12):3428-3436. doi: 10.1002/term.2256

19. Huang Y, Zhang Z, Bi F, *et al*. Personalized 3D-printed scaffolds with multiple bioactivities for bioroot. *Adv Healthc Mater*. 2023;12(28):2300625. doi: 10.1002/adhm.202300625

20. Rehman SRU, Augustine R, Zahid AA, Ahmen R, Tariq M, Hasan A. Reduced graphene oxide incorporated GelMA hydrogel promotes angiogenesis for wound healing applications. *Int J Nanomedicine*. 2019;14:9603-9617. doi: 10.2147/IJN.S218120

21. Sennerby L, Dasmah A, Larsson B, Iverhed M. Bone tissue responses to surface-modified zirconia implants: a histomorphometric and removal torque study in the rabbit. *Clin Implant Dent Relat Res*. 2005;7(Suppl 1):S13-S20. doi: 10.1111/j.1708-8208.2005.tb00070.x

22. Zhang J, Huang D, Liu S, *et al*. Zirconia toughened hydroxyapatite biocomposite formed by a DLP 3D printing process for potential bone tissue engineering. *Mater Sci Eng*. 2019;105:110054. doi: 10.1016/j.msec.2019.110054

23. Li R, Guo W, Yang B, *et al*. Human treated dentin matrix as a natural scaffold for complete human dentin tissue regeneration. *Biomaterials*. 2011;32(20):4525-4538. doi: 10.1016/j.biomaterials.2011.03.008

24. Lan T, Bi F, Xu Y, *et al*. PPAR-γ activation promotes xenogenic bioroot regenerationby attenuating the xenograft induced-oxidative stress. *Int J Oral Sci*. 2023;15(1):10. doi: 10.1038/s41368-023-00217-4

25. Chu CR, Szczodry M, Bruno S. Animal models for cartilage regeneration and repair. *Tissue Eng Part B Rev*. 2010;16(1):105-115. doi: 10.1089/ten.TEB.2009.0452

26. Tang H, Bi F, Chen G, *et al*. 3D-bioprinted recombination structure of Hertwig's epithelial root sheath cells and dental papilla cells for alveolar bone regeneration. *Int J Bioprint*. 2022;8(3):512. doi: 10.18063/ijb.v8i3.512

27. Ebrahimi M, Ojanen S, Mohammadi A, *et al*. Elastic, viscoelastic and fibril-reinforced poroelastic material properties of healthy and osteoarthritic human tibial cartilage. *Ann Biomed Eng*. 2019;47(4):953-966. doi: 10.1007/s10439-019-02213-4

28. Li J, Wang P, Xie Z, *et al*. TRAF4 positively regulates the osteogenic differentiation of mesenchymal stem cells by acting as an E3 ubiquitin ligase to degrade Smurf2. *Cell Death Differ*. 2019;26(12):2652-2666. doi: 10.1038/s41418-019-0328-3

29. Kim H, Park S, Kim K, Ku S, Seo J, Roh S. *Enterococcus faecium* L-15 cell-free extract improves the chondrogenic differentiation of human dental pulp stem cells. *Int J Mol Sci*. 2019;20(3):624. doi: 10.3390/ijms20030624

30. Wang T, Chen Y, Zhu X, *et al*. IFT80 and TRPA1 cooperatively regulate bone formation by calcium signaling in response to mechanical stimuli. *Metabolism*. 2025;166:156159. doi: 10.1016/j.metabol.2025.156159

31. Menendez M T TC, Wade K, *et al*. siRNA screening identifies the host hexokinase 2 (HK2) gene as an__important hypoxia-inducible transcription factor 1 (HIF-1) target gene in toxoplasma gondii-infected cells. *mBio*. 2015;6(3):e00462. doi: 10.1128/mBio.00462-15

32. Wang Z-Y, Yiu L, Li S-P, *et al*. Hypoxia inducible factor 1α promotes interleukin-1 receptor antagonist expression during hepatic ischemia-reperfusion injury. *World J Gastroenterol*. 2022;28(38):5573-5588.
doi: 10.3748/wjg.v28.i38.5573

33. Zayed M, Newby S, Misk N, Donnell R, Dhar M. Xenogenic implantation of equine synovial fluid-derived mesenchymal stem cells leads to articular cartilage regeneration. *Stem Cells Int*. 2018;2018:1073705.
doi: 10.1155/2018/1073705

34. Zheng ZY, Jiang T, Huang ZF, *et al*. Fatty acids derived from apoptotic chondrocytes fuel macrophages FAO through MSR1 for facilitating BMSCs osteogenic differentiation. *Redox Biol*. 2022;53:102326.
doi: 10.1016/j.redox.2022.102326

35. Liu ES, Raimann A, Chae BT, Martins JS, Baccarini M, Demay MB. c-Raf promotes angiogenesis during normal growth plate maturation. *Development*. 2016;143(2): 348-355.
doi: 10.1242/dev.127142

36. Zhou X, von der Mark K, Henry S, Norton W, Adams H, de Crombrugghe B. Chondrocytes transdifferentiate into osteoblasts in endochondral bone during development, postnatal growth and fracture healing in mice. *PLoS Genet*. 2014;10(12):e1004820.
doi: 10.1371/journal.pgen.1004820

37. van den Borne MPJ, Raijmakers NJH, Vanlauwe J, *et al*. International Cartilage Repair Society (ICRS) and Oswestry macroscopic cartilage evaluation scores validated for use in Autologous Chondrocyte Implantation (ACI) and microfracture1. *Osteoarthritis Cartilage*. 2007;15(12):1397-1402.
doi: 10.1016/j.joca.2007.05.005

38. Alberton P, Dugonitsch HC, Hartmann B, *et al*. Aggrecan hypomorphism compromisesarticular cartilage biomechanical propertiesand is associated with increased incidenceof spontaneous osteoarthritis. *Int J Mol Sci*. 2019;20(5):1008.
doi: 10.3390/ijms20051008

39. Chen S, Fu P, Wu H, Pei M. Meniscus, articular cartilage, and nucleus pulposus a comparative review of cartilage-like tissues in anatomy, development, and function. *Cell Tissue Res*. 2017;370(1):53-70.
doi: 10.1007/s00441-017-2613-0

40. Gannon AR, Nagel T, Bell AP, Avery NC, Kelly DJ. Postnatal changes to the mechanical properties of articular cartilage are driven by the evolution of its collagen network. *Eur Cells Mater*. 2015;29:105-123.
doi: 10.22203/eCM.v029a09

41. Richardson SM, Kalamegam G, Pushparaj PN, *et al*. Mesenchymal stem cells in regenerative medicine: focus on articular cartilage and intervertebral disc regeneration. *Methods*. 2016;99:69-81.
doi: 10.1016/j.ymeth.2015.09.015

42. Deng C, Zhu H, Li J, *et al*. Bioactive scaffolds for regeneration of cartilage and subchondral bone interface. *Theranostics*. 2018;8(7):1940-1955.
doi: 10.7150/thno.23674

43. Chen L, Yao F, Wang T, *et al*. Horizontal fissuring at the osteochondral interface: a novel and unique pathological feature in patients with obesity-related osteoarthritis. *Ann Rheum Dis*. 2020;79(6):811-818.
doi: 10.1136/annrheumdis-2020-216942

44. Slattery C, Kweon CY. Classifications in brief: outerbridge classification of chondral lesions. *Clin Orthop Relat Res*. 2018;476(10):2101-2104.
doi: 10.1007/s11999.0000000000000255

45. Pereira RC, Martinelli D, Cancedda R, Gentili C, Poggi A. Human articular chondrocytes regulate immune response by affecting directly T cell proliferation and indirectly inhibiting monocyte differentiation to professional antigen-presenting cells. *Front Immunol*. 2016;7:415.
doi: 10.3389/fimmu.2016.00415

46. Freeman FE, Kelly DJ. Tuning alginate bioink stifness and composition for controlled growth factor delivery and to spatially direct MSC fate within bioprinted tissues. *Sci Rep*. 2017;7(1):17042.
doi: 10.1038/s41598-017-17286-1

47. Aboul-Soud MAM, Alzahrani AJ, Mahmoud A. Induced pluripotent stem cells (iPSCs)—roles in regenerative therapies, disease modelling and drug screening. *Cells*. 2021;10(9):2319.
doi: 10.3390/cells10092319

48. Yamashita A, Morioka M, Yahara Y, *et al*. Generation of scaffoldless hyaline car tilaginous tissue from human iPSCs. *Stem Cell Reports*. 2015;4(3)404-418.
doi: 10.1016/j.stemcr.2015.01.016

49. Song H, Park K-H. Regulation and function of SOX9 during cartilage development and regeneration. *Semin Cancer Biol*. 2020;67(Pt 1):12-23.
doi: 10.1016/j.semcancer.2020.04.008

50. Jang Y, Jung H, Nam Y, *et al*. Centrifugal gravity-induced BMP4 induces chondrogenic differentiation of adiposederived stem cells via SOX9 upregulation. *Stem Cell Res Ther*. 2016;7(1):184.
doi: 10.1186/s13287-016-0445-6

51. Yan B Zhang Z, Wang X, *et al*. PLGA-PTMC-cultured bone mesenchymal stem cell scaffold enhances cartilage regeneration in tissue-engineered tracheal transplantation. *Artif Organs*. 2016;41(5):461-469.
doi: 10.1111/aor.12805

52. Wanjare M, Hou L, Nakayama KH, *et al*. Anisotropic microfibrous scaffolds enhance the organization and function of cardiomyocytes derived from induced pluripotent stem cells. *Biomater Sci*. 2017;5(8):1567-1578. doi: 10.1039/c7bm00323d

53. Schunck A, Kronz A, Fischer C, Buchhorn GH. Release of zirconia nanoparticles at the metal stem–bone cement interface in implant loosening of total hip replacements. *Acta Biomater*. 2016;31:412-424. doi: 10.1016/j.actbio.2015.11.044

54. Yang Y, Bao H, Chai Q, *et al*. Toxicity, biodistribution and oxidative damage caused by zirconia nanoparticles after intravenous injection. *Int J Nanomedicine*. 2019;14:5175-5186. doi: 10.2147/IJN.S197565

55. Eschweiler J, Horn N, Rath B, *et al*. The biomechanics of cartilage–an overview. *Life (Basel)*. 2021;11(4):302. doi: 10.3390/life11040302

56. Zhang M, Lu Q, Miller AH, Barnthouse NC, Wang J. Dynamic epigenetic mechanisms regulate age-dependent SOX9 expression in mouse articular cartilage. *Int J Biochem Cell Biol*. 2016;72:125-134. doi: 10.1016/j.biocel.2016.01.013

57. Korhonen RK, Laasanen MS, Töyräs J, *et al*. Comparison of the equilibrium response of articular cartilage in unconfined compression, confined compression and indentation. *J Biomech*. 2002;35(7):903-909. doi: 10.1016/s0021-9290(02)00052-0

58. Lehtola T, Nummenmaa E, Tuure L, *et al*. Dexamethasone attenuates the expression of MMP-13 in chondrocytes through MKP-1. *Int J Mol Sci*. 2022;23(7):3880. doi: 10.3390/ijms23073880

59. Chen C, Zhao W, Lu X, *et al*. AUP1 regulates lipid metabolism and induces lipidaccumulation to accelerate the progression of renal clearcell carcinoma. *Cancer Sci*. 2022;113(8):2600-2615. doi: 10.1111/cas.15445

60. Barkley LR, Hong HK, Kingsbury SR, James M, Stoeber K, Williams GH. Cdc6 is a rate-limiting factor for proliferative capacity during HL60 cell differentiation. *Exp Cell Res*. 2007;313(17):3789-3799. doi: 10.1016/j.yexcr.2007.07.004

61. Tu J, Wan C, Zhang F, *et al*. Genetic correction of Werner syndrome gene reveals impaired pro-angiogenic function and HGF insufficiency in mesenchymal stem cells. *Aging Cell*. 2020;19(5):e.13116. doi: 10.1111/acel.13116

62. Li Z, Yan G, Diao Q, *et al*. Transplantation of human endometrial perivascular cells with elevated CYR61 expression induces angiogenesis and promotes repair of a full-thickness uterine injury in rat. *Stem Cell Res Ther*. 2019;10(1):179. doi: 10.1186/s13287-019-1272-3

63. Gouttenoire J, Bougault C, Aubert-Foucher E, *et al*. BMP-2 and TGF-beta1 differentially control expression of type II procollagen and alpha 10 and alpha 11 integrins in mouse chondrocytes. *Eur J Cell Biol*. 2010;89(4):307-314. doi: 10.1016/j.ejcb.2009.10.018

64. Zhou N, Li Q, Lin X, *et al*. BMP2 induces chondrogenic differentiation, osteogenic differentiation and endochondral ossification in stem cells. *Cell Tissue Res*. 2016;366(1):101-111. doi: 10.1007/s00441-016-2403-0

65. Caron MJ, Welting TJ, Surtel DA, *et al*. BMP-2 and BMP-7: differential regulation of chondrogenic differentiation. *Osteoarthritis Cartilage*. 2012;20(1):S151. doi: 10.1016/j.joca.2012.02.220

66. Legendre F, Ollitrault D, Gomez-Leduc T, *et al*. Enhanced chondrogenesis of bone marrow-derived stem cells by using a combinatory cell therapy strategy with BMP-2/TGF-β1, hypoxia, and COL1A1/HtrA1 siRNAs. *Sci Rep*. 2017;7(1):3406. doi: 10.1038/s41598-017-03579-y

67. Chavez RD, Coricor G, Perez J, Seo HS, Serra R. SOX9 protein is stabilized by TGF-beta and regulates PAPSS2 mRNA expression in chondrocytes. *Osteoarthritis Cartilage*. 2017;25(2):332-340. doi: 10.1016/j.joca.2016.10.007

68. Tew SR, Clegg PD. Analysis of post transcriptional regulation of SOX9 mRNA during in vitro chondrogenesis. *Tissue Eng Part A*. 2011;17(13-14):1801-1807. doi: 10.1089/ten.TEA.2010.0579

69. Stegen S, Laperre K, Eelen G, *et al*. HIF-1alpha metabolically controls collagen synthesis and modification in chondrocytes. *Nature*. 2019;565(7740):511-515. doi: 10.1038/s41586-019-0874-3

70. Guo W, Gong K, Shi H, *et al*. Dental follicle cells and treated dentin matrix scaffold for tissue engineering the tooth root. *Biomaterials*. 2012;33(5):1291-1302. doi: 10.1016/j.biomaterials.2011.09.068

71. Idaszek J, Costantini M, Karlsen TA, *et al*. 3D bioprinting of hydrogel constructs with cell and material gradients for the regeneration of full-thickness chondral defect using a microfluidic printing head. *Biofabrication*. 2019;11(4):044101. doi: 10.1088/1758-5090/ab2622

72. Zhang B, Huang J, Narayan RJ. Gradient scaffolds for osteochondral tissue engineering and regeneration. *J Mater Chem B*. 2020;8(36):8149-8170. doi: 10.1039/d0tb00688b

73. Corrado F, Di Maio L, Palmero P, *et al*. Vat photo-polymerization 3D printing of gradient scaffolds for osteochondral tissue regeneration. *Acta Biomater*. 2025;200:67-86. doi: 10.1016/j.actbio.2025.05.042